Preprints.org

Article

Not peer-reviewed version

Microwave field induced changes in Raman modes and magnetic force images of antiferromagnetic NiO films

Farkhad G. Aliev *, Diego Caso, Aida Serrano, Miriam Jaafar, Pilar Prieto, César González-Ruano, Akashdeep Kamra

Posted Date: 3 October 2023

doi: 10.20944/preprints202310.0112.v1

Keywords: NiO; domain walls; microwave; antiferromagnet; Raman

Preprints.org is a free multidiscipline platform providing preprint service that is dedicated to making early versions of research outputs permanently available and citable. Preprints posted at Preprints.org appear in Web of Science, Crossref, Google Scholar, Scilit, Europe PMC.

Copyright: This is an open access article distributed under the Creative Commons Attribution License which permits unrestricted use, distribution, and reproduction in any medium, provided the original work is properly cited.

Preprints (www.preprints.org) | NOT PEER-REVIEWED | Posted: 3 October 2023 doi:10.20944/preprints202310.0112.v1

Disclaimer/Publisher's Note: The statements, opinions, and data contained in all publications are solely those of the individual author(s) and contributor(s) and not of MDPI and/or the editor(s). MDPI and/or the editor(s) disclaim responsibility for any injury to people or property resulting from any ideas, methods, instructions, or products referred to in the content.

Article

Microwave Field Induced Changes in Raman Modes and Magnetic Force Images of Antiferromagnetic NiO Films

Diego Caso [1], Aída Serrano [2], Miriam Jaafar [1,3,4], Pilar Prieto [5], Akashdeep Kamra [6], César González-Ruano [1] and Farkhad G. Aliev [1,3,4,*]

1 Departamento de Física de la Materia Condensada C03, Universidad Autónoma de Madrid, Madrid 28049, Spain
2 Departamento de Electrocerámica, Instituto de Cerámica y Vidrio (ICV), CSIC, Madrid 28049, Spain
3 Instituto Nicolás Cabrera (INC), Universidad Autónoma de Madrid, Madrid 28049, Spain
4 Condensed Matter Physics Institute (IFIMAC), Universidad Autónoma de Madrid, Madrid 28049, Spain
5 Departamento de Física Aplicada, M-12 and Instituto Nicolás Cabrera (INC), Universidad Autónoma de Madrid, Madrid 28049, Spain
6 Departamento de Física Teorica de la Materia Condensada C-05, and Condensed Matter Physics Institute (IFIMAC), Universidad Autónoma de Madrid, Madrid 28049, Spain
* Correspondence: farkhad.aliev@uam.es

Abstract: Effective control of domain walls or magnetic textures in antiferromagnets promises to enable robust, fast, and non-volatile memories. The lack of net magnetic moment in antiferromagnets implies the need for creative ways to achieve such a manipulation. Here, we investigate changes in magnetic force microscopy (MFM) imaging and in magnon-related mode in Raman spectroscopy of virgin NiO films under a microwave pump. After the MFM and Raman studies, a combined action of broadband microwave (0.01-20 GHz, power scanned from −20 to 5 dBm) and magnetic field (up to 3 kOe) were applied to virgin epitaxial (111) NiO and (100) NiO films grown on (0001) Al_2O_3 and (100) MgO substrates, following which the MFM and Raman studies were repeated. We observed a suppression of the magnon-related Raman mode subsequent to the microwave exposure. Based on MFM imaging, this effect appears to be caused by the suppression of large antiferromagnetic domain walls due to the possible excitation of antiferromagnetic spin oscillations localized within the antiferromagnetic domain walls.

Keywords: NiO; domain walls; microwave; antiferromagnet; Raman

1. Introduction

Recently, antiferromagnets (AFM) and particularly insulating thin AFM films have attracted ample attention due to their potentially unmatched characteristics, which could allow the development of spintronic devices with speeds reaching the THz domain [1,2], ultra-low Gilbert damping [3] and good spin current conduction [4]. Another unique merit of AFMs is the minuteness of the stray fields [5] and consequently, the difficulty to control the domain walls (AFM DWs) by the laboratory magnetic fields. The presence of AFM DWs may substantially restrict the propagation length of magnons in antiferromagnets [6]. The effective manipulation of magnetic textures in antiferromagnets, and specifically those related with AFM DWs, is central to the emerging field of AFM spintronics [7].

A number of schemes to control the AFM DWs have been proposed recently. Among them are thermal [8] or strong field gradients [9], field pulses [10] or spin waves [11] with specific helicity [12]. Néel spin torque to drive AFM DWs should be effective only for specific antiferromagnets with locally broken inversion symmetry [13]. The practical realization of this mechanism via electrical switching of antiferromagnets by (high energy loss) DC currents [14] has been under debate [15,16]. Robust control over AFM DWs, which is critical for effective spin wave propagation over micrometer distances [6], still remains a great challenge [13] and alternative techniques are required to probe and manipulate non-trivial AFM order [5].

© 2023 by the author(s). Distributed under a Creative Commons CC BY license.

Preprints (www.preprints.org) | NOT PEER-REVIEWED | Posted: 3 October 2023 doi:10.20944/preprints202310.0112.v1

NiO is an archetype antiferromagnet for room-temperature applications, and has recently been the focus of intensive research as it shows AFM resonance in the THz range in the absence of external magnetic field [17,18], which nonetheless could be tuned by an external field of a few Tesla [19]. In the last few years, there have been some suggestions to explore the THz spin dynamics with the aim of creating AFM memories [20,21]. However, the domain structure of NiO is very complex, as at least 12 orientation domains including twin (T) and spin (S) domains [22] and double domain walls [23] have been reported, with sizes of about microns to tenths of a micron depending on the oxygen annealing conditions [24].

Interestingly, recent studies reveal that spin current transmission in AFM insulators can be mediated by coherent spin waves not only in THz [25] but also in the GHz range [26,27]. This observation confirms previous reports on spin angular momentum transfer at the GHz excitation range without phase control [28–31] and inertial dynamics of antiferromagnets [32]. The GHz dynamics of solitons or AFM DWs [11] could be excited either by circular or linearly polarized drives capable of producing a net AFM DW drift in colinear antiferromagnets [33,34]. Besides evanescent [27] and thermal spin waves [4,31,35,36] underlying the spin transport through AFMs, an intriguing possibility for low-frequency spin waves' propagation exists due to the modes localized around the domain walls [37].

Recently, laser pulses have been shown to modify the structure of AFM DWs, creating antiferromagnetic 180° domains in NiO/Pt bilayers [38]. Here, we investigate the possibility of influencing the AFM DW structure in virgin NiO films by the application of a broadband (10 MHz-20 GHz) microwaves (MW) with power up to 5 dBm and an in-plane magnetic field up to 3 kOe at room temperature. We use magnetic force microscopy and confocal micro-Raman spectroscopy to study the possible effect of the microwave excitation on the AFM DW magnetic textures in NiO.

2. Structural characterization of the virgin films

2.1. Film growth, XRD and RBS characterization

NiO thin films can be grown epitaxially on oxide single-crystal substrates. (100) NiO epitaxial films have been usually grown on (100) MgO substrates, while (111) MgO and c-cut Al_2O_3 substrates have been used to obtain epitaxial (111) NiO films. In this last case, a bi-epitaxial growth with both in plane relationships: $[\bar{1}\bar{1}0]NiO//[00\bar{1}0]Al_2O_3$ and $[\bar{1}1\bar{2}]NiO//[2\bar{1}\bar{1}0]Al_2O_3$ has been reported [39,40]. In this work, NiO thin films were deposited on (0001) Al_2O_3 and (100) MgO substrates by ion beam sputtering using Ar^+ ions from a 3 cm Kaufmann-type ion source of a pure nickel (99.99%) target in a controlled atmosphere of oxygen and argon. The NiO thin films were deposited in a vacuum chamber with a base pressure of 2×10^{-5} Pa. During the deposition, the pressure was maintained between 1.8×10^{-2} and 4.1×10^{-2} Pa and the substrates were rotated at 2 rpm to increase the homogeneity of the deposit. The substrate temperature during deposition, the oxygen partial pressure, as well as the sputtering conditions, i.e. current density of sputtered Ni atoms, J_{sp}, and energy of the sputtering Ar^+ ions, E_{sp}, are shown on Table 1.

Preprints (www.preprints.org) | NOT PEER-REVIEWED | Posted: 3 October 2023 doi:10.20944/preprints202310.0112.v1

Table 1. NiO thin films deposition parameters: substrate temperature, oxygen partial pressure, Ar^+ energy and sputter current density. The thickness determined by RBS quantification and out-of-plane lattice parameter determined by XRD are also included.

	NiO(1)	**NiO(2)**	**NiO(3)**	**NiO(4)/MgO**
Substrate	Al_2O_3(0001)	Al_2O_3(0001)	Al_2O_3(0001)	MgO(100)
$T_{substrate}$(K)	633	718	798	798
PO_2(Pa)	1.3×10^{-2}	2.2×10^{-2}	2.8×10^{-2}	2.8×10^{-2}
J_{sp} (mA/cm^2)	1.6	1.4	1.1	1.1
E_{sp} (eV)	650	650	650	650
Thickness (nm)	244	228	195	207
Deposition rate (A/s)	0.33	0.33	0.27	0.26
Lattice parameter (nm)	0.428	0.423	0.426	0.425

The crystal structure and texture of the different films deposited on (0001) Al_2O_3 and (100) MgO substrates were analyzed by X-ray diffraction (XRD) in a $\theta/2\theta$ configuration using a PANanalytical X'Pert MPD system and Cu-Kα radiation. Figure 1a shows the XRD scans corresponding to the NiO (111) peak region for the films grown on (0001) Al_2O_3 substrates.It should be noted that only NiO (111), NiO (222) and Al_2O_3 (006) diffraction peaks can be distinguished in the complete diffractogram (not shown) indicating the epitaxial character of the growth. For the NiO(2) film exclusively, in addition to the NiO (111) peak, a very small NiO (200) peak also appears at $\sim 43.2^\circ$ (not shown in the figure), indicating that this film is highly (111) oriented, but can have a polycrystalline nature. Figure 1b shows the XRD scan of the NiO film grown on (100) MgO substrate in which a shoulder at $\sim 42.6^\circ$ corresponding to NiO (200) diffraction plane can be distinguished in the intense (200) peak from the MgO substrate. The lattice mismatch between NiO films and (0001) Al_2O_3 substrate has been calculated following the well-known crystallographic orientation relationships and the domain matching epitaxy proposed by Lee et al. [39] and have been plotted on Figure 1c. The Figure also includes the lattice mismatch for NiO(4) film grown on (100) MgO substrate following the epitaxial relationship: [100]NiO/[100]MgO.

Preprints (www.preprints.org) | NOT PEER-REVIEWED | Posted: 3 October 2023 doi:10.20944/preprints202310.0112.v1

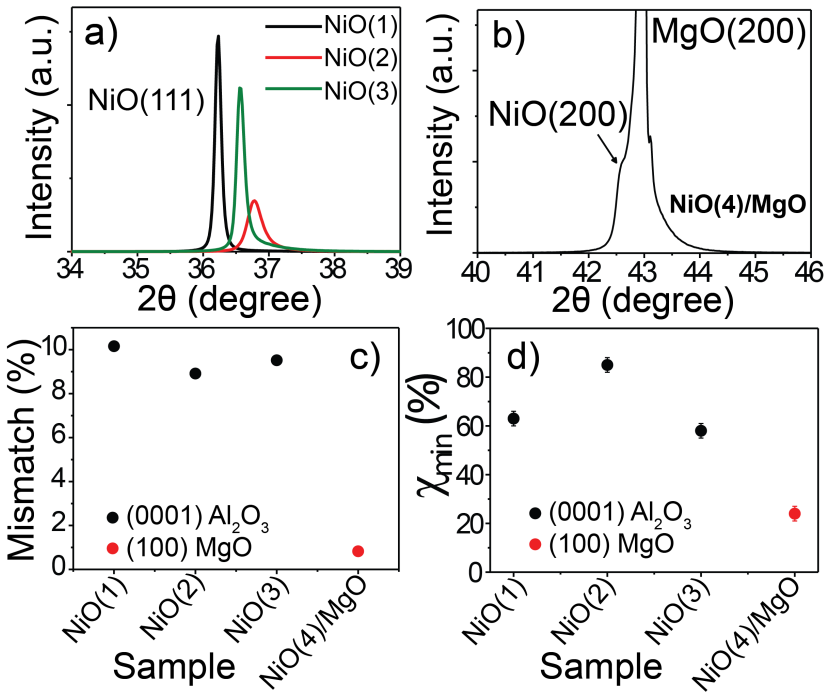

Figure 1. XRD diffraction patterns of (a) (111) NiO films grown on (0001) Al_2O_3 substrate and (b) (100) NiO film grown on (100) MgO substrate. (c) Lattice mismatch with the substrate and (d) minimum yield ratio obtained from the channeling and random RBS spectra for the NiO films grown on (0001) Al_2O_3 and (100) MgO substrates.

In order to explore the elemental distribution, thickness and epitaxial quality of the deposited thin films, Rutherford backscattering spectrometry (RBS) was performed under both random and channeling conditions using $^4He^+$ at 1.8 MeV in a 5 MV tandem accelerator [41]. The ion fluence for the Rutherford backscattering was 20 μC. A silicon barrier detector, at a scattering angle of 170.5°, measured the backscattering ions while a three-axis goniometer was employed to control the crystal position. The elements present in the thin films, as well as in the substrate, were identified in the spectra (not shown here), where the width of each peak corresponds to the relative thickness. The distribution and quantification of the various elements was determined with the SIMNRA simulation software package. If the material of the film is oriented along the substrate and the direction of the incident $^4He^+$ particles is aligned in the substrate orientation direction, most of the particles will pass through the channel or empty space available within the crystal lattice leading to lower yield. The energetic ions can move into the crystals, penetrating much deeper if the atoms in the crystal are directed in some specific crystal directions. The decrease of the yield when the film is aligned is an indication of the epitaxial character of the films. Figure 1d shows the minimum yield ratio between channeling and random spectra for the different NiO films. The lowest value is found in NiO(4)/MgO film, which is in good agreement with the lowest mismatch found in this film as it is observed on Figure 1c.

2.2. Atomic Force Microscopy characterization

Atomic force microscopy measurements were carried out on different virgin NiO films (see Figure 2) using an instrument from Nanotec Electronica S.L. controlled by the WSxM software [42]. Both typical images and root mean square (RMS) roughness analysis are in general agreement with XRD and RBS characterization, pointing towards the most flat surface in NiO(4)/MgO and the highest roughness in NiO(2) film.

Preprints (www.preprints.org) | NOT PEER-REVIEWED | Posted: 3 October 2023 doi:10.20944/preprints202310.0112.v1

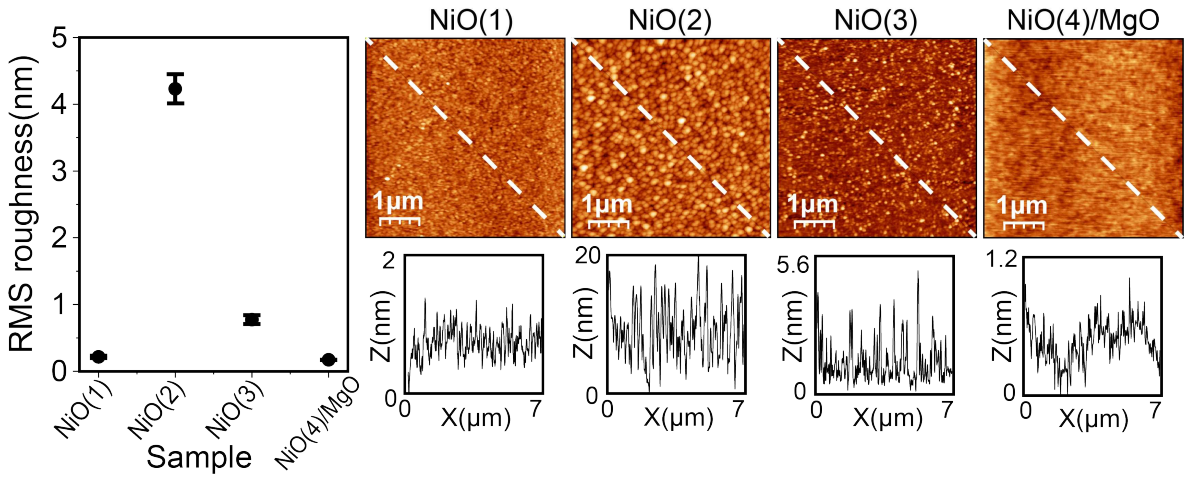

Figure 2. Atomic force microscopy characterization of the NiO films. RMS roughness of the films is measured on several images showing an average value. Error bars constitute the standard deviation of the measurements. All of the samples are quite flat and free from surface defects, specially NiO(1) and NiO(4)/MgO. NiO(2) presents much more roughness than the rest of the samples.

2.3. Micro-Raman characterization

Confocal micro-Raman experiments were conducted on as-grown NiO films, and the same films immediately after microwave exposure. The measurements were collected using a confocal Raman microscope (CRM) WITec ALPHA 300RA at room temperature with a Nd:YAG linearly polarized laser (532 nm). The Raman spectra were recorded in the range of 0˜3600 cm^{-1}, using an objective with a numerical aperture of 0.95 and a laser excitation power of 3.2 mW to avoid any damage to the films. The NiO films were investigated on the plane (XY scans) and in-depth (XZ scans) regions. The collected spectra were analyzed with the WITec Project Plus software.

NiO is widely studied by Raman spectroscopy due to its room-temperature AFM behavior. Raman spectra recorded from different NiO films deposited on (0001) Al_2O_3 and MgO (100) substrates are shown in Figure 3. The Raman signal is collected from the confocal plane of the film with the highest intensity, averaging several Raman spectra from different regions. Complementarily, a Raman study was performed in both types of substrates in order to discriminate their specific Raman signal. The Raman signal related to the Al_2O_3 substrate can be identified around 420 and 754 cm^{-1} on the NiO films (see Appendix A). The MgO substrate doesn't show Raman modes, but a fluorescence signal at higher wavenumbers (from 2700 cm^{-1}) that does not interfere with the active modes of NiO.

Preprints (www.preprints.org) | NOT PEER-REVIEWED | Posted: 3 October 2023 doi:10.20944/preprints202310.0112.v1

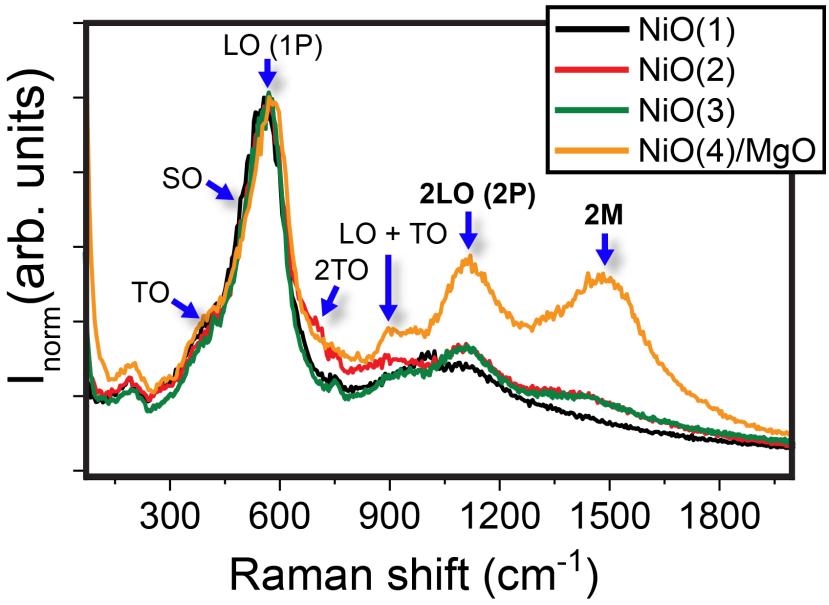

Figure 3. Resolved Raman modes for all the analyzed NiO films in the virgin state. The active modes are in agreement with previous reports [43,44], corroborating the good quality of the films. The 2LO (2*P*) and 2M modes are specially visible in the NiO(4)/MgO sample. Raman spectra are normalized to the LO mode (1*P*).

The active Raman modes are in full agreement with previous reports [43,44], confirming the generally good quality of the NiO films. The first-order phonon modes, longitudinal optical (LO), 1*P* and transverse optical (TO) are inactive Raman modes in the perfect rock salt-like structure, and can appear due to the rhombohedral lattice distortion and the presence of impurity atoms in the crystal lattice. Their intensity is strongly dependent on the stoichiometric ratio in the lattice. The surface optical (SO) phonon mode is also marked in the Raman spectra and represents a well-known indicator to identify surface defects and roughness [44]. This band is practically imperceptible due to the good quality and low roughness of the films, confirmed by the XRD and atomic force microscopy results. At higher wavenumbers, the 2TO, LO+TO and the 2LO(2*P*) overtones are identified, as well as the two-magnon mode (2*M*). The 2LO (2*P*) Raman mode at 1120 cm^{-1} can be attributed to biaxial strain in NiO films, and the quotient $I_{1P(LO)}/I_{2P(2LO)}$ can be considered an inverse figure of merit that provides information about the crystal quality of the films [45]. The lowest intensity quotient is measured for NiO(4)/MgO and the largest one for NiO(1) (see Figure 3). Finally, the 2*M* band (two-magnon mode) at about 1500 cm^{-1} is measurable as a fingerprint of AFM ordering, identifying the largest intensity for NiO(4)/MgO and the lowest one for NiO(1). Additionally, a redshift is observed along with the intensity decrease of the 2*M* mode, which can be explained by a reduction in the AFM coupling via Ni-O super exchange interaction [46].

2.4. Magnetic force microscopy characterization

All the measurements were performed at ambient conditions using a scanning force microscope from Nanotec Electronica S.L. controlled by the WSxM software [42]. Commercial MFM probes from Nanosensors PPP-MFMR and Budget Sensors (MultiM-75) were used. The magnetic probes are always calibrated before and after each experiments to verify their performance, especially when no MFM signal is detected. Amplitude modulation method was carried out enabling the phase-locked loop (PLL) to track the resonance frequency of the oscillating cantilever and the magnetic signal was therefore recorded in the frequency shift channel, in Hz. In addition, electrostatic force microscopy images were performed with a PtIr metallic tip from Nanosensors.

Preprints (www.preprints.org) | NOT PEER-REVIEWED | Posted: 3 October 2023 doi:10.20944/preprints202310.0112.v1

3. Results

In order to present the main findings on the influence of the microwave response on magnetic textures in initially virgin NiO films, we will mainly concentrate on the description of the data obtained on NiO(3) and NiO(4)/MgO films, for which detailed MFM imaging was carried out.

3.1. Influence of MWs on MFM images in virgin NiO films

MFM is one of the most powerful tools to investigate magnetic materials at the nanoscale [47]. However, imaging AFM domains or domain walls with this technique still remains a challenge. Nitrogen Vacancy (NV) magnetometry [5], Spin-Polarized STM [48], or the combination of MFM with Magnetic Exchange Force Microscopy [49] are some of the imaging methods that are emerging to study the AFM order. Nonetheless, MFM was used to investigate the influence of crystallographic defects in AFM materials such as NiO [50].

We correlated our results with MFM images and confocal Raman spectroscopy in order to verify if the microwave excitations affect the magnetic textures. Two types of experiments were carried out along this line. First, we investigated both MFM and micro-Raman on the virgin samples, which had not yet been exposed to the application of any microwave drive. Then, the same measurements were performed right after (less than 1 hour) the application of the maximum available microwave excitation of 5 dBm.

Within the resolution of our MFM setup, magnetic textures were invisible in the virgin NiO(4)/MgO films, probably due to too low values of the stray fields from AFM DWs in the most perfect NiO films.

On the other hand, MFM imaging on NiO(3) (see Figure 4a) reveals the presence of irregular magnetic textures similar to those typically observed in synthetic [51] or natural Ni antiferromagnets [23]. Separate checks using Kelvin Probe force microscopy [52] with electrostatic tip have proven that the MFM images are related with magnetic and not electrostatic interactions, as could potentially happen when imaging weakly magnetic insulators.

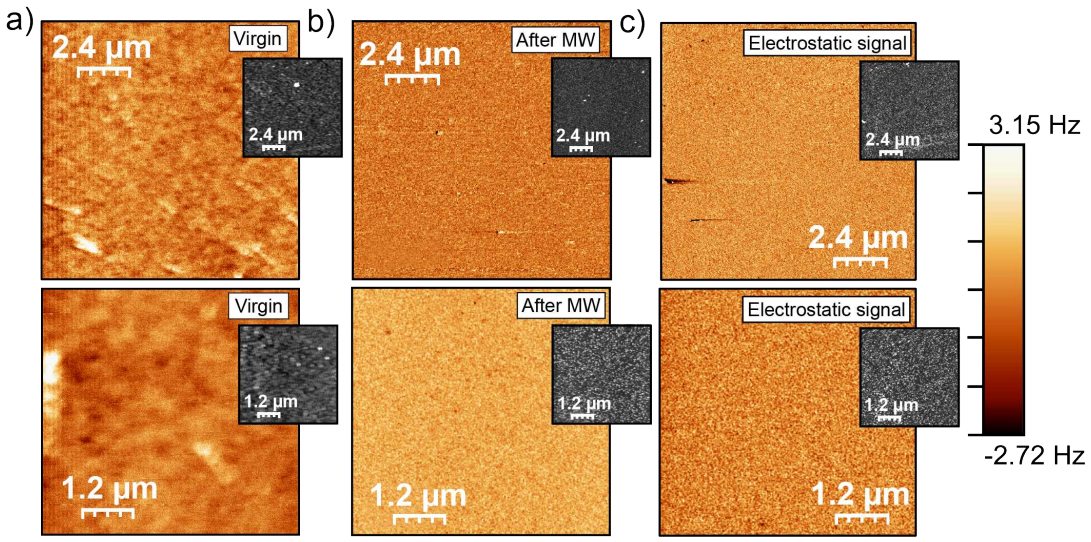

Figure 4. Two MFM resolved images of different regions (up and down panels) of the NiO(3) sample, (a) before and (b) after the application of a MW excitation. The magnetic texture observed in the virgin state disappears after the MW application, in line with our proposed interpretation. (c) shows the electrostatic image, which suggest a purely magnetic nature of the observed features. The black and white insets are the topographical map of each region.

We have also investigated MFM images on the same NiO(3) film two weeks after the maximum microwave drive was last applied. Our measurements could not detect any large-scale magnetic

Preprints (www.preprints.org) | NOT PEER-REVIEWED | Posted: 3 October 2023 doi:10.20944/preprints202310.0112.v1

textures, but revealed a much more localized response probably related to dislocation-induced weak ferromagnetism, previously reported in NiO [50].

3.2. Influence of microwaves on Raman modes in virgin NiO films

In order to further explore a possible correlation between magnetic textures and the irradiated MWs, we carried out confocal micro-Raman experiments.

The typical Raman signal for NiO was collected [43,44], with differences in the Raman modes depending on the film. As shown in Figure 5, the effect of the MW application on the Raman spectra was recorded, and an in-depth analysis of the films was also carried out. Figures 5a,b and 6a-d show, in the example of NiO(4)/MgO, how the Raman modes change with the film depth. This could be related to a structural variation from the interface with the substrate towards the film surface, which is confirmed by the channeling characterization (see Figure 5d): there is an agreement between the yield ratio of aligned to random spectra, that increases from the surface to the interface, and the intensity of the 2M Raman mode. Figure 5c analyzes the relative intensity of the $2P$ and $2M$ overtones with respect to the $1P$ band for all the films investigated, and shows their variation within the next few hours after the application of a 5 dBm microwave field. The variation is specially pronounced for the NiO(4)/MgO sample. Based on the observed MFM reduction of large scale AFM DWs, we propose that this reduction of the amplitude of Raman active modes is related to AF magnons ($2M$ mode) and reflects structural imperfections (the intensity relation between $1P$ and $2P$ bands is proportional to the degree of structural order) [45,46], which could be linked with the magnetostrictive character of AFM DWs in NiO [23]. As a consequence, once the microwave drive has perturbed the complex AFM DW order, the system tends to recover its complexity by moving and creating large scale AFM DWs and moving back towards the energy minimum during the Raman experiments. Such slow AFM DW dynamics and rearrangements (which could take place in a timescale of weeks) and related lattice distortions may be responsible for the relative suppression of the $2P$ and $2M$ Raman modes in the NiO films previously excited by the microwaves.

Preprints (www.preprints.org) | NOT PEER-REVIEWED | Posted: 3 October 2023 doi:10.20944/preprints202310.0112.v1

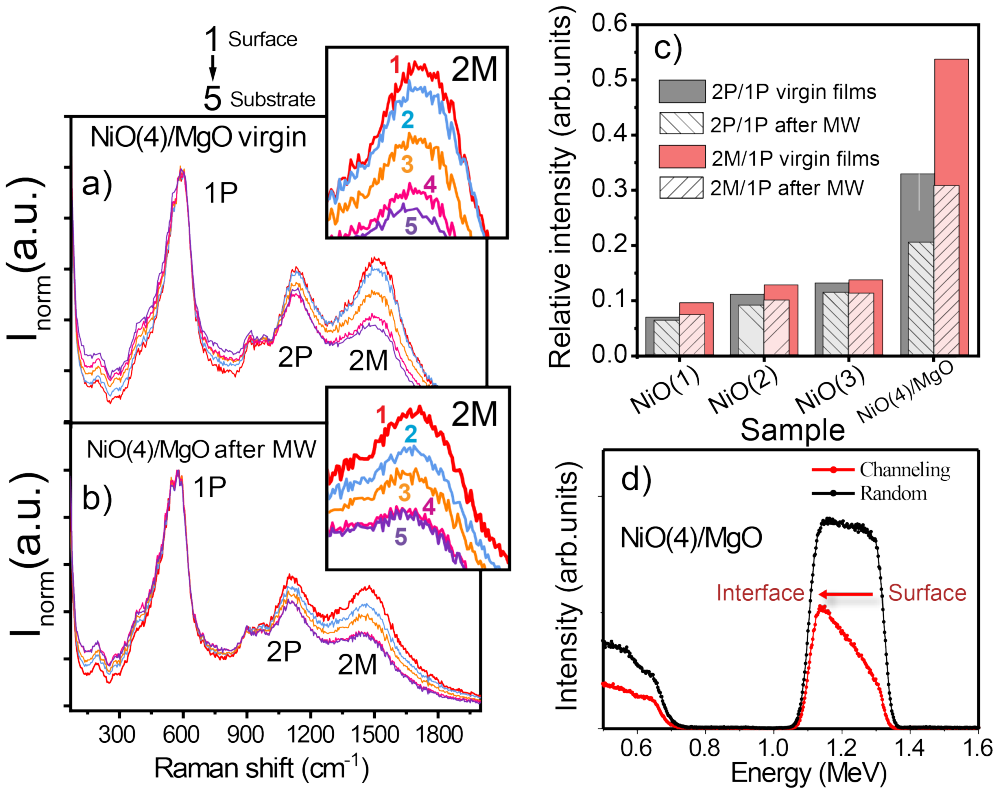

Figure 5. Resolved Raman spectra in the in-depth direction (XZ plane) for the NiO(4)/MgO sample (a) in its virgin state and (b) right after being put through a maintained microwave drive of 5 dBm. The normalization of the intensity signal is done adjusting the 1*P* band. The assignation of the 1*P*, 2*P* and 2*M* active modes is marked on the figure. Raman spectra correspond to equidistant points in the depth profile of the film from the film surface (1) to the substrate interface (5). This analysis shows extraordinary variation of the 2*P* and 2*M* modes in the depth coordinate. (c) 2*P*/1*P* and 2*M*/1*P* relative intensity on the virgin films and after the application of MW. There is a correlation between a reduction of the intensity of the 2*P* and 2*M* modes and the application of MW for all of the analyzed samples. The NiO(4)/MgO sample is especially sensible to the effect of the MW, partially since 2*P* and 2*M* modes are very manifested. (d) Channeling and random RBS spectra of the NiO(4)/MgO sample.

Preprints (www.preprints.org) | NOT PEER-REVIEWED | Posted: 3 October 2023 doi:10.20944/preprints202310.0112.v1

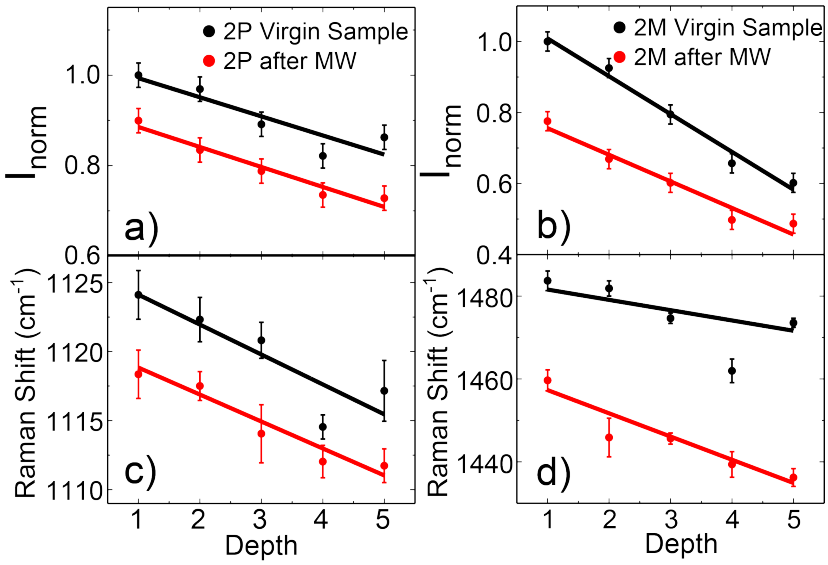

Figure 6. Behavior of the 2P (a,c) and 2M (b,d) Raman modes in the NiO(4)/MgO sample against the depth of the analysis before and after a continuous application of MW field. (a,b) Intensity of the modes, normalized by the maximum value before the MW pumping. (c,d) Raman shift of the modes' peaks.

4. Discussion and Conclusions

Let us discuss a possible mechanism behind the absorption of GHz range microwaves by the AF NiO films with magnons in the THz range. Following Refs. [37], we consider the existence of low-frequency excitations in NiO localized within the magnetic textures (AFM DWs). Indeed, the dispersion relation for the soft branch is predicted to be gapless due to string-like domain wall excitation in AFMs. These localized modes should be similar to Winter magnons [53,54] excited along domain walls in ferromagnets.

A high-power microwave excitation may lead to irreversible changes in the magnetic texture of the NiO films via localized heating of the DWs. Such a scenario is suggested by the difference in the Raman and MFM responses seen on the samples before and after a high-power MW excitation was applied. We therefore relate these irreversible changes in magnetic textures with the localized power absorption by spin waves confined around AFM domain walls/textures [37].

We note that the temperature variation of the substrate side during the application of the MW power up to +5 dBm did not exceed $\sim$ 0.5 K, which is close to the accuracy limit of our infrared thermometer given the different kind of materials involved and the room temperature fluctuations during the experiments.

This upper limit is in agreement with numerical simulations made with COMSOL (Appendix B) and with simple analytical estimations based on the maximum power dissipated by the MWs into the NiO sample. Therefore, we don't exclude that, in addition to the direct excitation of DWs (magnetic textures) by the MWs, there could be a localized heating close to those textures where the MW losses should be enhanced. This additional local heating (which is hardly detectable by the IR thermometer or the COMSOL simulations) could help the system to thermally overcome the energy barrier between its textured state and the global minimum energy state with a more spatially homogeneous magnetic order. This effect, in combination with the direct excitation of AF-DWs by the MWs, could be the underlying cause of the observed reduction of DWs after exposure to microwave excitation.

Finally, we point out that microwave permeability experiments as a function of MW power carried out on a virgin NiO film (see Appendix C) showed a resonant response between 15 and 17 GHz, with an increasing magnitude and a frequency shift once the MW power exceeds -15 dBm. Similar measurements carried out on the substrate (MgO) side of the sample showed a background nearly

Preprints (www.preprints.org) | NOT PEER-REVIEWED | Posted: 3 October 2023 doi:10.20944/preprints202310.0112.v1

independent of the MW power. We believe that this kind of MW-induced excitations could account for the above-described changes in Raman modes and MFM images of the AFM NiO films.

Author Contributions: Conceptualization F.G.A. and P.P.; methodology, A.S., D.C., M.J, F.G.A., and P.P.; software, D.C. and C.G-R.; validation, A.S., F.G.A., D.C. and C.G-R.; formal analysis, A.S., M.J., D.C. and P.P.; investigation, D.C., C.G-R., P.P., A.K. and F.G.A; resources, F.G.A and P.P.; data curation, M.J., A.S. and D.C.; writing–original draft preparation, F.G.A., D.C., P.P., A.S., M.J. and A.K.; writing-review and editing, F.G.A., D.C., C.G-R. and A.K.; visualization, D.C. and C.G-R.; supervision, F.G.A.; project administration, F.G.A. and P.P.; funding acquisition, F.G.A. and P.P., All authors have read and agreed to the published version of the manuscript.

Funding: This research was funded by Spanish Ministerio de Ciencia e Innovación (PID2021-124585NB-C32, PID2021-124585NB-C33, PID2021-122980OA-C53 and TED2021-130196B-C22). F.G.A. also acknowledges financial support from the Spanish Ministerio de Ciencia e Innovación through the María de Maeztu Programme for Units of Excellence in R&D (CEX2018-000805-M) and "Acción financiada por la Comunidad de Madrid en el marco del convenio plurianual con la Universidad Autónoma de Madrid en Línea 3: Excelencia para el Profesorado Universitario." P.P. acknowledges Comunidad de Madrid and Universidad Autonoma de Madrid under the V PRICIT program through the Project SI3/PJI/2021-00393. A.S. acknowledges the financial support from MICINN for a Ramón y Cajal contract (RYC2021-031236-I), which is funded by the Recovery, Transformation and Resilience plan.

Institutional Review Board Statement: Not applicable

Informed Consent Statement: Not applicable

Data Availability Statement: Data will be made available upon reasonable request.

Conflicts of Interest: The authors declare no conflict of interest

Appendix A. Control Raman experiments on the MgO and Al_2O_3 substrates

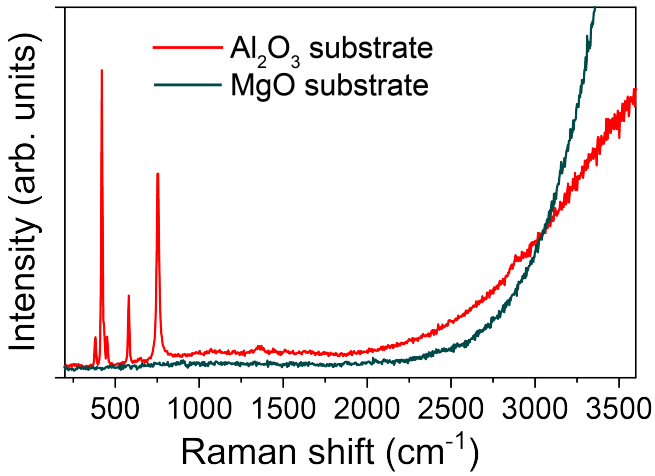

Figure A1. Raman signal of the MgO and Al_2O_3 substrates used in our NiO samples.

Raman spectroscopy was conducted on the used substrates. In the case of the MgO, no Raman band was detected, only a fluorescence signal above 2700 cm^{-1}. The Al_2O_3 substrate presented several Raman modes, with the highest intensity for those located around 420 and 754 cm^{-1}, which is observed in the Raman signal measured in the samples with this specific substrate.

Appendix B. COMSOL simulations on the temperature provided by the MW heating on the sample

COMSOL simulations were conducted to obtain the temperature increase on the NiO(4)/MgO sample when exposed to MW radiation. It is important to notice that these simulations are limited by the possible magnetic textures in the sample, which are not replicated. To emulate the MW irradiation, we implemented a homogeneous heat source on the NiO side of the sample. On the other boundaries, we allowed surface-to-ambient radiation ($T_{ambient} = 300K$).

Preprints (www.preprints.org) | NOT PEER-REVIEWED | Posted: 3 October 2023 doi:10.20944/preprints202310.0112.v1

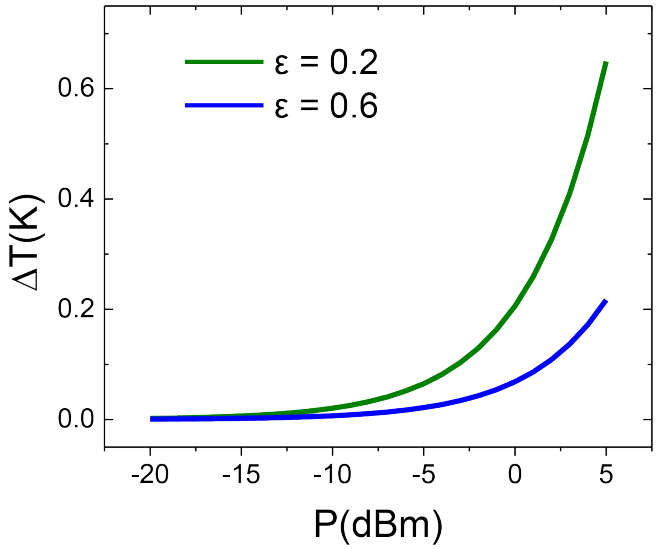

Figure A2. COMSOL simulations of the temperature difference between the NiO(4)/MgO and the room temperature for different irradiated MW powers. Curves for upper ($\epsilon = 0.6$) and lower ($\epsilon = 0.2$) surface emissivity bounds are presented.

We observe that the maximum temperature increase does not exceed 0.7 K in the lower surface emissivity bound, and 0.3 K in the upper bound, as seen in Figure A2. This is in agreement with our previous temperature estimations. However, it is important to acknowledge that localized heating within the magnetic textures cannot be ruled out, as previously suggested.

Preprints (www.preprints.org) | NOT PEER-REVIEWED | Posted: 3 October 2023 doi:10.20944/preprints202310.0112.v1

Appendix C. Microwave transmission measurements as a function of power

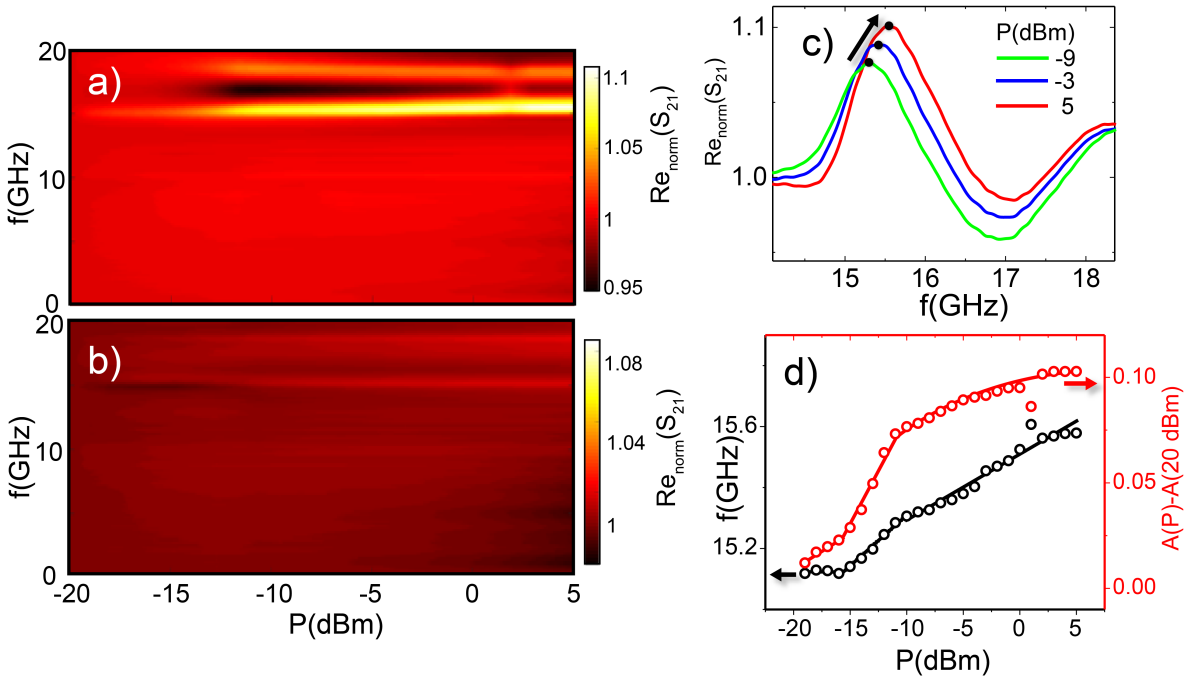

Figure A3. Real part of the scattering matrix element S_{21} normalized to −20 dBm, measured for the NiO(4)/MgO sample as a function of the MW power. (a) Measurement done with the NiO side facing the CPW. (b) Measurement done with the substrate (MgO) facing the CPW. (c) Cross-sections of the peak around 15 GHz seen in part (a) for different MW powers, illustrating its displacement. (d) Frequency and amplitude of the 15-16 GHz peak against the MW power. The peak position was resolved by fitting the peak in the $Re_{norm}(S_{21})$ cross-sections to a Lorentzian curve.

In order to probe the dynamic magnetic response of the different samples, a vector network analyzer (VNA) high-frequency setup was used (see [54] for details), placing the films directly on top of a coplanar waveguide (CPW).

In these MW experiments, driving AC fields of up to 5 dBm were applied to the NiO(4)/MgO sample on its virgin state. The microwave frequency covered a frequency range between 10 MHz and 20 GHz. Transmission measurements were made sweeping this frequency at zero bias DC field and averaging 20 measurements for each dBm to ensure noise reduction. The scattering matrix element S_{21} measured by the VNA, which is the relation between the magnitude and phase of the input signal sent to the CPW and the received signal, is indicative of the transmission in the system [55].

To ensure a response related to the antiferromagnetic sample, control measurements were performed on the substrate face and the NiO face of the sample. Figure A3 shows a zero field measurement of the normalized real part of the S_{21} scattering matrix element of the NiO(4)/MgO virgin sample, for a MW power from −20 dBm to 5 dBm. Figure A3a represents the dynamic response of the NiO, while panel b corresponds to the MgO substrate. Panels c,d represent the analysis of the peak amplitude and frequency observed in the NiO side as a function of the applied MW power.

References

1. Satoh, T.; Cho, S.J.; Iida, R.; Shimura, T.; Kuroda, K.; Ueda, H.; Ueda, Y.; Ivanov, B.A.; Nori, F.; Fiebig, M. Spin Oscillations in Antiferromagnetic NiO Triggered by Circularly Polarized Light. *Physical Review Letters* **2010**, *105*. doi:10.1103/physrevlett.105.077402.

Preprints (www.preprints.org) | NOT PEER-REVIEWED | Posted: 3 October 2023 doi:10.20944/preprints202310.0112.v1

2. Moriyama, T.; Hayashi, K.; Yamada, K.; Shima, M.; Ohya, Y.; Ono, T. Intrinsic and extrinsic antiferromagnetic damping in NiO. *Physical Review Materials* **2019**, *3*. doi:10.1103/physrevmaterials.3.051402.
3. Kampfrath, T.; Sell, A.; Klatt, G.; Pashkin, A.; Mährlein, S.; Dekorsy, T.; Wolf, M.; Fiebig, M.; Leitenstorfer, A.; Huber, R. Coherent terahertz control of antiferromagnetic spin waves. *Nature Photonics* **2010**, *5*, 31–34. doi:10.1038/nphoton.2010.259.
4. Lebrun, R.; Ross, A.; Bender, S.A.; Qaiumzadeh, A.; Baldrati, L.; Cramer, J.; Brataas, A.; Duine, R.A.; Kläui, M. Tunable long-distance spin transport in a crystalline antiferromagnetic iron oxide. *Nature* **2018**, *561*, 222–225. doi:10.1038/s41586-018-0490-7.
5. Hedrich, N.; Wagner, K.; Pylypovskyi, O.V.; Shields, B.J.; Kosub, T.; Sheka, D.D.; Makarov, D.; Maletinsky, P. Nanoscale mechanics of antiferromagnetic domain walls. *Nature Physics* **2021**, *17*, 574–577. doi:10.1038/s41567-020-01157-0.
6. Ross, A.; Lebrun, R.; Gomonay, O.; Grave, D.A.; Kay, A.; Baldrati, L.; Becker, S.; Qaiumzadeh, A.; Ulloa, C.; Jakob, G.; Kronast, F.; Sinova, J.; Duine, R.; Brataas, A.; Rothschild, A.; Kläui, M. Propagation Length of Antiferromagnetic Magnons Governed by Domain Configurations. *Nano Letters* **2019**, *20*, 306–313. doi:10.1021/acs.nanolett.9b03837.
7. Song, C.; You, Y.; Chen, X.; Zhou, X.; Wang, Y.; Pan, F. How to manipulate magnetic states of antiferromagnets. *Nanotechnology* **2018**, *29*, 112001. doi:10.1088/1361-6528/aaa812.
8. Kim, S.K.; Tchernyshyov, O.; Tserkovnyak, Y. Thermophoresis of an antiferromagnetic soliton. *Physical Review B* **2015**, *92*. doi:10.1103/physrevb.92.020402.
9. Zhang, Y.L.; Chen, Z.Y.; Yan, Z.R.; Chen, D.Y.; Fan, Z.; Qin, M.H. Staggered field driven domain walls motion in antiferromagnetic heterojunctions. *Applied Physics Letters* **2018**, *113*. doi:10.1063/1.5042567.
10. Bodnar, S.Y.; Skourski, Y.; Gomonay, O.; Sinova, J.; Kläui, M.; Jourdan, M. Magnetoresistance Effects in the Metallic Antiferromagnet Mn_2Au. *Physical Review Applied* **2020**, *14*. doi:10.1103/physrevapplied.14.014004.
11. Yu, W.; Lan, J.; Xiao, J. Polarization-selective spin wave driven domain-wall motion in antiferromagnets. *Physical Review B* **2018**, *98*. doi:10.1103/physrevb.98.144422.
12. Qaiumzadeh, A.; Kristiansen, L.A.; Brataas, A. Controlling chiral domain walls in antiferromagnets using spin-wave helicity. *Physical Review B* **2018**, *97*. doi:10.1103/physrevb.97.020402.
13. Gomonay, O.; Jungwirth, T.; Sinova, J. High Antiferromagnetic Domain Wall Velocity Induced by Néel Spin-Orbit Torques. *Physical Review Letters* **2016**, *117*. doi:10.1103/physrevlett.117.017202.
14. Wadley, P.; Howells, B.; Železný, J.; Andrews, C.; Hills, V.; Campion, R.P.; Novák, V.; Olejník, K.; Maccherozzi, F.; Dhesi, S.S.; Martin, S.Y.; Wagner, T.; Wunderlich, J.; Freimuth, F.; Mokrousov, Y.; Kuneš, J.; Chauhan, J.S.; Grzybowski, M.J.; Rushforth, A.W.; Edmonds, K.W.; Gallagher, B.L.; Jungwirth, T. Electrical switching of an antiferromagnet. *Science* **2016**, *351*, 587–590. doi:10.1126/science.aab1031.
15. Meer, H.; Schreiber, F.; Schmitt, C.; Ramos, R.; Saitoh, E.; Gomonay, O.; Sinova, J.; Baldrati, L.; Kläui, M. Direct Imaging of Current-Induced Antiferromagnetic Switching Revealing a Pure Thermomagnetoelastic Switching Mechanism in NiO. *Nano Letters* **2020**, *21*, 114–119. doi:10.1021/acs.nanolett.0c03367.
16. Churikova, A.; Bono, D.; Neltner, B.; Wittmann, A.; Scipioni, L.; Shepard, A.; Newhouse-Illige, T.; Greer, J.; Beach, G.S.D. Non-magnetic origin of spin Hall magnetoresistance-like signals in Pt films and epitaxial NiO/Pt bilayers. *Applied Physics Letters* **2020**, *116*. doi:10.1063/1.5134814.
17. Keffer, F.; Kittel, C. Theory of Antiferromagnetic Resonance. *Physical Review* **1952**, *85*, 329–337. doi:10.1103/physrev.85.329.
18. Safin, A.R.; Nikitov, S.A.; Kirilyuk, A.I.; Kalyabin, D.V.; Sadovnikov, A.V.; Stremoukhov, P.A.; Logunov, M.V.; Popov, P.A. Excitation of Terahertz Magnons in Antiferromagnetic Nanostructures: Theory and Experiment. *Journal of Experimental and Theoretical Physics* **2020**, *131*, 71–82. doi:10.1134/s1063776120070110.
19. Wang, Z.; Kovalev, S.; Awari, N.; Chen, M.; Germanskiy, S.; Green, B.; Deinert, J.C.; Kampfrath, T.; Milano, J.; Gensch, M. Magnetic field dependence of antiferromagnetic resonance in NiO. *Applied Physics Letters* **2018**, *112*. doi:10.1063/1.5031213.
20. Olejník, K.; Seifert, T.; Kašpar, Z.; Novák, V.; Wadley, P.; Campion, R.P.; Baumgartner, M.; Gambardella, P.; Němec, P.; Wunderlich, J.; Sinova, J.; Kužel, P.; Müller, M.; Kampfrath, T.; Jungwirth, T. Terahertz electrical writing speed in an antiferromagnetic memory. *Science Advances* **2018**, *4*. doi:10.1126/sciadv.aar3566.
21. Chirac, T.; Chauleau, J.Y.; Thibaudeau, P.; Gomonay, O.; Viret, M. Ultrafast antiferromagnetic switching in NiO induced by spin transfer torques. *Physical Review B* **2020**, *102*. doi:10.1103/physrevb.102.134415.

Preprints (www.preprints.org) | NOT PEER-REVIEWED | Posted: 3 October 2023 doi:10.20944/preprints202310.0112.v1

22. Arai, K.; Okuda, T.; Tanaka, A.; Kotsugi, M.; Fukumoto, K.; Ohkochi, T.; Nakamura, T.; Matsushita, T.; Muro, T.; Oura, M.; Senba, Y.; Ohashi, H.; Kakizaki, A.; Mitsumata, C.; Kinoshita, T. Three-dimensional spin orientation in antiferromagnetic domain walls of NiO studied by x-ray magnetic linear dichroism photoemission electron microscopy. *Physical Review B* **2012**, *85*. doi:10.1103/physrevb.85.104418.
23. Weber, N.B.; Ohldag, H.; Gomonaj, H.; Hillebrecht, F.U. Magnetostrictive Domain Walls in Antiferromagnetic NiO. *Physical Review Letters* **2003**, *91*. doi:10.1103/physrevlett.91.237205.
24. Sänger, I.; Pavlov, V.V.; Bayer, M.; Fiebig, M. Distribution of antiferromagnetic spin and twin domains in NiO. *Physical Review B* **2006**, *74*. doi:10.1103/physrevb.74.144401.
25. Hortensius, J.R.; Afanasiev, D.; Matthiesen, M.; Leenders, R.; Citro, R.; Kimel, A.V.; Mikhaylovskiy, R.V.; Ivanov, B.A.; Caviglia, A.D. Coherent spin-wave transport in an antiferromagnet. *Nature Physics* **2021**, *17*, 1001–1006. doi:10.1038/s41567-021-01290-4.
26. Qiu, Z.; Li, J.; Hou, D.; Arenholz, E.; N'Diaye, A.T.; Tan, A.; ichi Uchida, K.; Sato, K.; Okamoto, S.; Tserkovnyak, Y.; Qiu, Z.Q.; Saitoh, E. Spin-current probe for phase transition in an insulator. *Nature Communications* **2016**, *7*. doi:10.1038/ncomms12670.
27. Dabrowski, M.; Nakano, T.; Burn, D.M.; Frisk, A.; Newman, D.G.; Klewe, C.; Li, Q.; Yang, M.; Shafer, P.; Arenholz, E.; Hesjedal, T.; van der Laan, G.; Qiu, Z.Q.; Hicken, R.J. Coherent Transfer of Spin Angular Momentum by Evanescent Spin Waves within Antiferromagnetic NiO. *Physical Review Letters* **2020**, *124*. doi:10.1103/physrevlett.124.217201.
28. Hahn, C.; de Loubens, G.; Naletov, V.V.; Youssef, J.B.; Klein, O.; Viret, M. Conduction of spin currents through insulating antiferromagnetic oxides. *EPL (Europhysics Letters)* **2014**, *108*, 57005. doi:10.1209/0295-5075/108/57005.
29. Wang, H.; Du, C.; Hammel, P.C.; Yang, F. Antiferromagnonic Spin Transport from $Y_3Fe_5O_{12}$ into NiO. *Physical Review Letters* **2014**, *113*. doi:10.1103/physrevlett.113.097202.
30. Wang, H.; Du, C.; Hammel, P.C.; Yang, F. Spin transport in antiferromagnetic insulators mediated by magnetic correlations. *Physical Review B* **2015**, *91*. doi:10.1103/physrevb.91.220410.
31. Moriyama, T.; Takei, S.; Nagata, M.; Yoshimura, Y.; Matsuzaki, N.; Terashima, T.; Tserkovnyak, Y.; Ono, T. Anti-damping spin transfer torque through epitaxial nickel oxide. *Applied Physics Letters* **2015**, *106*. doi:10.1063/1.4918990.
32. Kimel, A.V.; Ivanov, B.A.; Pisarev, R.V.; Usachev, P.A.; Kirilyuk, A.; Rasing, T. Inertia-driven spin switching in antiferromagnets. *Nature Physics* **2009**, *5*, 727–731. doi:10.1038/nphys1369.
33. Gerasimchuk, V.S.; Gorobets, Y.I.; Goujon-Durand, S. Domain-wall motion in antiferromagnets in microwave fields. *Physical Review B* **1994**, *49*, 9608–9612. doi:10.1103/physrevb.49.9608.
34. Chen, Z.Y.; Yan, Z.R.; Zhang, Y.L.; Qin, M.H.; Fan, Z.; Lu, X.B.; Gao, X.S.; Liu, J.M. Microwave fields driven domain wall motions in antiferromagnetic nanowires. *New Journal of Physics* **2018**, *20*, 063003. doi:10.1088/1367-2630/aac68e.
35. Han, J.; Zhang, P.; Bi, Z.; Fan, Y.; Safi, T.S.; Xiang, J.; Finley, J.; Fu, L.; Cheng, R.; Liu, L. Birefringence-like spin transport via linearly polarized antiferromagnetic magnons. *Nature Nanotechnology* **2020**, *15*, 563–568. doi:10.1038/s41565-020-0703-8.
36. Wimmer, T.; Kamra, A.; Gückelhorn, J.; Opel, M.; Geprägs, S.; Gross, R.; Huebl, H.; Althammer, M. Observation of Antiferromagnetic Magnon Pseudospin Dynamics and the Hanle Effect. *Phys. Rev. Lett.* **2020**, *125*, 247204. doi:10.1103/PhysRevLett.125.247204.
37. Flebus, B.; Ochoa, H.; Upadhyaya, P.; Tserkovnyak, Y. Proposal for dynamic imaging of antiferromagnetic domain wall via quantum-impurity relaxometry. *Physical Review B* **2018**, *98*. doi:10.1103/physrevb.98.180409.
38. Meer, H.; Wust, S.; Schmitt, C.; Herrgen, P.; Fuhrmann, F.; Hirtle, S.; Bednarz, B.; Rajan, A.; Ramos, R.; Niño, M.A.; Foerster, M.; Kronast, F.; Kleibert, A.; Rethfeld, B.; Saitoh, E.; Stadtmüller, B.; Aeschlimann, M.; Kläui, M. Laser-Induced Creation of Antiferromagnetic 180-Degree Domains in NiO/Pt Bilayers. *Advanced Functional Materials* **2023**, *33*. doi:10.1002/adfm.202213536.
39. Lee, J.H.; Kwon, Y.H.; Kong, B.H.; Lee, J.Y.; Cho, H.K. Biepitaxial Growth of High-Quality Semiconducting NiO Thin Films on (0001) Al_2O_3 Substrates: Microstructural Characterization and Electrical Properties. *Cryst. Growth Des.* **2012**, *12*, 2495–2500. doi:10.1021/cg3001174.
40. Becker, M.; Polity, A.; Klar, P.J. NiO films on sapphire as potential antiferromagnetic pinning layers. *Journal of Applied Physics* **2017**, *122*. doi:10.1063/1.4991601.

Preprints (www.preprints.org) | NOT PEER-REVIEWED | Posted: 3 October 2023 doi:10.20944/preprints202310.0112.v1

41. Redondo-Cubero, A.; Borge, M.J.G.; Gordillo, N.; Gutiérrez, P.C.; Olivares, J.; Casero, R.P.; Ynsa, M.D. Current status and future developments of the ion beam facility at the centre of micro-analysis of materials in Madrid. *The European Physical Journal Plus* **2021**, *136*. doi:10.1140/epjp/s13360-021-01085-9.
42. Horcas, I.; Fernández, R.; Gómez-Rodríguez, J.M.; Colchero, J.; Gómez-Herrero, J.; Baro, A.M. WSXM: A software for scanning probe microscopy and a tool for nanotechnology. *Review of Scientific Instruments* **2007**, *78*. doi:10.1063/1.2432410.
43. Aytan, E.; Debnath, B.; Kargar, F.; Barlas, Y.; Lacerda, M.M.; Li, J.X.; Lake, R.K.; Shi, J.; Balandin, A.A. Spin-phonon coupling in antiferromagnetic nickel oxide. *Applied Physics Letters* **2017**, *111*. doi:10.1063/1.5009598.
44. Sunny, A.; Balasubramanian, K. Raman Spectral Probe on Size-Dependent Surface Optical Phonon Modes and Magnon Properties of NiO Nanoparticles. *The Journal of Physical Chemistry C* **2020**, *124*, 12636–12644. doi:10.1021/acs.jpcc.0c02638.
45. Budde, M.; Tschammer, C.; Franz, P.; Feldl, J.; Ramsteiner, M.; Goldhahn, R.; Feneberg, M.; Barsan, N.; Oprea, A.; Bierwagen, O. Structural, optical, and electrical properties of unintentionally doped NiO layers grown on MgO by plasma-assisted molecular beam epitaxy. *Journal of Applied Physics* **2018**, *123*. doi:10.1063/1.5026738.
46. Feldl, J.; Budde, M.; Tschammer, C.; Bierwagen, O.; Ramsteiner, M. Magnetic characteristics of epitaxial NiO films studied by Raman spectroscopy. *Journal of Applied Physics* **2020**, *127*. doi:10.1063/5.0006085.
47. Kazakova, O.; Puttock, R.; Barton, C.; Corte-León, H.; Jaafar, M.; Neu, V.; Asenjo, A. Frontiers of magnetic force microscopy. *Journal of Applied Physics* **2019**, *125*. doi:10.1063/1.5050712.
48. Bode, M.; Vedmedenko, E.Y.; von Bergmann, K.; Kubetzka, A.; Ferriani, P.; Heinze, S.; Wiesendanger, R. Atomic spin structure of antiferromagnetic domain walls. *Nature Materials* **2006**, *5*, 477–481. doi:10.1038/nmat1646.
49. Geng, Y.; Das, H.; Wysocki, A.L.; Wang, X.; Cheong, S.W.; Mostovoy, M.; Fennie, C.J.; Wu, W. Direct visualization of magnetoelectric domains. *Nature Materials* **2013**, *13*, 163–167. doi:10.1038/nmat3813.
50. Sugiyama, I.; Shibata, N.; Wang, Z.; Kobayashi, S.; Yamamoto, T.; Ikuhara, Y. Ferromagnetic dislocations in antiferromagnetic NiO. *Nature Nanotechnology* **2013**, *8*, 266–270. doi:10.1038/nnano.2013.45.
51. Herranz, D.; Guerrero, R.; Villar, R.; Aliev, F.G.; Swaving, A.C.; Duine, R.A.; van Haesendonck, C.; Vavra, I. Anomalous low-frequency noise in synthetic antiferromagnets: Possible evidence of current-induced domain-wall motion. *Physical Review B* **2009**, *79*. doi:10.1103/physrevb.79.134423.
52. Jaafar, M.; Iglesias-Freire, O.; Serrano-Ramón, L.; Ibarra, M.R.; de Teresa, J.M.; Asenjo, A. Distinguishing magnetic and electrostatic interactions by a Kelvin probe force microscopy–magnetic force microscopy combination. *Beilstein Journal of Nanotechnology* **2011**, *2*, 552–560. doi:10.3762/bjnano.2.59.
53. Winter, J.M. Bloch Wall Excitation. Application to Nuclear Resonance in a Bloch Wall. *Physical Review* **1961**, *124*, 452–459. doi:10.1103/physrev.124.452.
54. Aliev, F.G.; Awad, A.A.; Dieleman, D.; Lara, A.; Metlushko, V.; Guslienko, K.Y. Localized domain-wall excitations in patterned magnetic dots probed by broadband ferromagnetic resonance. *Physical Review B* **2011**, *84*. doi:10.1103/physrevb.84.144406.
55. Müller, M.; Liensberger, L.; Flacke, L.; Huebl, H.; Kamra, A.; Belzig, W.; Gross, R.; Weiler, M.; Althammer, M. Temperature-Dependent Spin Transport and Current-Induced Torques in Superconductor-Ferromagnet Heterostructures. *Physical Review Letters* **2021**, *126*. doi:10.1103/physrevlett.126.087201.

Disclaimer/Publisher's Note: The statements, opinions and data contained in all publications are solely those of the individual author(s) and contributor(s) and not of MDPI and/or the editor(s). MDPI and/or the editor(s) disclaim responsibility for any injury to people or property resulting from any ideas, methods, instructions or products referred to in the content.